

**Manuscript version: Author's Accepted Manuscript**

The version presented in WRAP is the author's accepted manuscript and may differ from the published version or Version of Record.

**Persistent WRAP URL:**

<http://wrap.warwick.ac.uk/164099>

**How to cite:**

Please refer to published version for the most recent bibliographic citation information. If a published version is known of, the repository item page linked to above, will contain details on accessing it.

**Copyright and reuse:**

The Warwick Research Archive Portal (WRAP) makes this work by researchers of the University of Warwick available open access under the following conditions.

© 2022, Elsevier. Licensed under the Creative Commons Attribution-NonCommercial-NoDerivatives 4.0 International <http://creativecommons.org/licenses/by-nc-nd/4.0/>.



**Publisher's statement:**

Please refer to the repository item page, publisher's statement section, for further information.

For more information, please contact the WRAP Team at: [wrap@warwick.ac.uk](mailto:wrap@warwick.ac.uk).

# Interface engineered Sb<sub>2</sub>O<sub>3</sub>/W<sub>18</sub>O<sub>49</sub> heterostructure for enhanced visible-light-driven photocatalytic N<sub>2</sub> reduction

Xiangchao Hui <sup>a</sup>, Lifan Li <sup>b</sup>, Qineng Xia <sup>b</sup>, Song Hong <sup>a</sup>, Leiduan Hao <sup>a</sup>, Alex W. Robertson <sup>c</sup>, Zhenyu Sun <sup>a,\*</sup>

<sup>a</sup> *State Key Laboratory of Organic-Inorganic Composites, College of Chemical Engineering, Beijing University of Chemical Technology, Beijing 100029, P. R. China*

<sup>b</sup> *College of Biological, Chemical Science and Engineering, Jiaying University, Jiaying, Zhejiang 314001, P. R. China*

<sup>c</sup> *Department of Physics, University of Warwick, Coventry, CV4 7AL, U. K.*

## Abstract

The direct photochemical N<sub>2</sub> reduction reaction boasts the potential for clean and sustainable NH<sub>3</sub> manufacturing, yet achieving this remains a significant challenge. To activate and cleave the nonpolar N≡N bond and accelerate the transport and separation of charge carriers during photocatalysis, the design and facile synthesis of active, robust, cheap, and earth-abundant photocatalysts is crucial. Here, we demonstrate efficient and stable visible light fixation of N<sub>2</sub> to NH<sub>3</sub> by constructing a novel heterostructure consisting of two-dimensional Sb<sub>2</sub>O<sub>3</sub> nanosheets and one-dimensional W<sub>18</sub>O<sub>49</sub> nanowires. A remarkable NH<sub>3</sub> production rate of up to 731 μg<sub>NH<sub>3</sub></sub> h<sup>-1</sup> g<sub>cat.</sub><sup>-1</sup> is attained in visible light over the nanocomposite without cocatalyst, 5.5-fold and 3.4-fold improvement over that of discrete Sb<sub>2</sub>O<sub>3</sub> and W<sub>18</sub>O<sub>49</sub> respectively, which also significantly exceeds many previous reported

---

\* Corresponding author. Tel.: +86 13301308339. E-mail address: sunzy@mail.buct.edu.cn

photocatalytic systems. The superior photocatalytic performance can be attributed to the unique structure of the composites, which provides ample exposed surface catalytic sites with a high density of oxygen vacancies, promoting the adsorption and activation of  $N_2$  molecules to form  $^*NNH$ . Equally importantly, the interface between  $Sb_2O_3$  and  $W_{18}O_{49}$  greatly facilitates charge carrier migration and separation. Further density functional theory calculations manifest that the interfacial metal sites on  $Sb_2O_3/W_{18}O_{49}$  serve as the main active centers which possess a strong donating electron ability to the empty  $N_2$  antibonding orbitals to trigger the following  $NH_3$  synthesis. This work provides a simple and effective method to modify metal oxides for enhancing  $N_2$  photofixation.

**Keywords:**  $N_2$  reduction; Photocatalysis;  $NH_3$ ; Heterostructure

## 1. Introduction

Ammonia ( $NH_3$ ) is an indispensable raw material for modern industry and agriculture, and thus plays a central role in human survival and economic development [1–3]. With continuously increasing world population and escalating urbanization, the global annual production of  $NH_3$  amounted to 150 million tons in 2019, making it the second-most produced chemical in the world after sulfuric acid. Currently,  $NH_3$  is still predominantly fabricated through the traditional Haber-Bosch process, a catalysed reaction between nitrogen and hydrogen gases. This century-old route demands harsh reaction conditions (i.e., 15–25 MPa and 300–500 °C) and use of hydrogen gas obtained from steam reforming, leading to high capital costs for this energy-intensive process and necessitates centralization of production. The excessive consumption of fossil fuels and the consequent high  $CO_2$

emissions of this reaction render the development of a green and sustainable protocol to yield  $\text{NH}_3$  particularly urgent [4–6]. To this end, there is a growing interest in the field of semiconductor photocatalysis employing renewable solar energy as the driving force for on-site ammonia production under ambient conditions [7,8]. However,  $\text{N}_2$  is a thermodynamically stable and kinetically inert molecule with a strong  $\text{N}\equiv\text{N}$  bond ( $\approx 940.1 \text{ kJ mol}^{-1}$ ) and low polarizability, making it unfavorable for adsorption and activation.

Since Schrauzer et al. first reported the pioneering work of Fe-doped  $\text{TiO}_2$  semiconductor for photocatalytic  $\text{N}_2$  reduction in 1977 [9], extensive attempts have been made to expand the family of photocatalysts for ameliorating the reaction conditions and improving the conversion efficiency [10]. Despite the great strides in this direction that have been taken [11,12], photocatalytic artificial  $\text{N}_2$  fixation still suffers from the weak reduction ability of photogenerated electrons and the rapid recombination of photoexcited carriers. Moreover, the energy efficiency is far from ideal owing to the insufficient electron transfer from photocatalyst to  $\text{N}_2$  molecules ( $\text{N}_2 + \text{e}^- \rightarrow \text{N}_2^{\bullet-}$ ,  $-4.2 \text{ V}$ ;  $\text{N}_2 + \text{H}^+ + \text{e}^- \rightarrow \text{*N}_2\text{H}$ ,  $-3.2 \text{ V}$  vs. normal hydrogen electrode, NHE). It is widely acknowledged that the prerequisite step of the  $\text{N}_2$  reduction reaction (NRR) is to break the  $\text{N}\equiv\text{N}$  bond. Although transition metal-based semiconductors can interact with  $\text{N}_2$  through the formation of N–metal bonds to facilitate the  $\text{N}\equiv\text{N}$  dissociation [13–15], subsequent rapid recombination of photoexcited electron-hole pairs in single materials hinders the proton-coupled electron transfer process. To alleviate this issue, interface and heterostructure design in different dimensions and components provides an intriguing route to efficiently improve the separation of photogenerated carriers [16–18].

Tungsten suboxides ( $\text{WO}_{3-x}$ ) have been shown to facilitate the adsorption and

activation of N<sub>2</sub> molecules [19] and lower the NRR thermodynamic overpotential [20]. Monoclinic W<sub>18</sub>O<sub>49</sub> is of particular interest because of its large oxygen deficiency, suitable bandgap energy, and tunable electronic structure as well as the existence of mixed-valence W ions, endowing it with distinctive photocatalytic performance [21–24]. To accommodate the large energy band of N<sub>2</sub>, tailoring surface oxygen vacancies [25] and doping of tungsten oxides with heteroatoms [26] are effective strategies, which can increase the number of active sites for N<sub>2</sub> chemisorption and provide adequate energetic electrons for N<sub>2</sub> reduction. Nevertheless, the solar-to-NH<sub>3</sub> yield rate achieved thus far remains insufficient. It is desirable to design and develop advanced WO<sub>3-x</sub>-based catalysts to accelerate the transport of photogenerated electrons toward N<sub>2</sub> molecules, thereby boosting N<sub>2</sub> activation and reduction.

Emerging two-dimensional (2D) materials possess a highly exposed active surface and fast charge transfer to inhibit the recombination of electrons and holes, showing potential in photocatalysis. 2D antimony (Sb, a group-VA element) behaves as a semiconductor in the visible range with tunable bandgaps regulated by altering thickness. It has a relatively high carrier mobility when thinned to single and few layers [27,28]. The tunability in defect type, concentration, and surface/edge termination attained by controlling synthetic methods makes 2D Sb an intriguing photocatalytic material. Owing to similar valence electron structure, Sb and N atoms tend to have strong p orbital hybridization, which would promote the N<sub>2</sub> protonation [29,30]. Meanwhile, the low-valence Sb species may also polarize the chemisorbed N<sub>2</sub> molecules and accelerate electron transfer from coordinatively unsaturated sites to N<sub>2</sub> adsorbates, rendering cleavage of the triple bond more feasible.

Here we report the design and synthesis of a novel well-defined heterostructure comprising 2D Sb<sub>2</sub>O<sub>3</sub> nanosheets and one-dimensional (1D) W<sub>18</sub>O<sub>49</sub> nanowires that have extended intimate interfaces. The as-obtained 2D/1D nanocomposites enable ambient photocatalytic N<sub>2</sub> reduction to produce ammonia in the visible light regime. The photocatalytic properties can be readily regulated by tuning the interface of the two components and their ratio, affording an NH<sub>3</sub> yield rate as high as 731  $\mu\text{g}_{\text{NH}_3} \text{ h}^{-1} \text{ g}_{\text{cat.}}^{-1}$ , much higher than that of both single W<sub>18</sub>O<sub>49</sub> and oxidized Sb nanosheets. The recovered catalyst can be reused at least five times without significant loss of activity. Moreover, based on microstructural characterization and photocatalytic assays, it is suggested that the extensive interfaces between the Sb<sub>2</sub>O<sub>3</sub> and W<sub>18</sub>O<sub>49</sub> effectively enhanced the charge carrier transport and separation. Additionally, the oxygen vacancies in ultrathin W<sub>18</sub>O<sub>49</sub> nanowires facilitated binding and activation of N<sub>2</sub> molecules. The charge redistribution between Sb<sub>2</sub>O<sub>3</sub> and W<sub>18</sub>O<sub>49</sub> boosts activation of the inert N $\equiv$ N triple bond, which accelerates the rate-determining proton-coupled electron transfer step with a lower energy barrier.

## **2. Experimental section**

### *2.1. Materials and chemicals*

All chemicals used in this work were of analytical grade and used without further treatments. Bulk antimony was purchased from Nanjing MKNANO Tech. Co., Ltd. ([www.mukenano.com](http://www.mukenano.com)). Tungsten (VI) chloride (WCl<sub>6</sub>), Sb<sub>2</sub>O<sub>3</sub>, NH<sub>4</sub>Cl, NaOH, methanol, isopropanol (IPA), ethanol, NaClO, and C<sub>5</sub>FeN<sub>6</sub>Na<sub>2</sub>O were provided by Aladdin. HCl (37%) was bought from Beijing Chemical Works. Nafion solution (5 wt%) was provided by Alfa Aesar. Deionized water (18.2 M $\Omega$ ·cm) was

obtained from a Millipore system and used in all experiments. Nitrogen gas and argon gas were both supplied by Beijing Haipu Gas Co., Ltd.

## *2.2. Production of antimonene nanosheets (2D Sb)*

Bulk antimony was first pulverized into powder in a mortar using a pestle. Then 2 g of the crushed powder was added in 400 mL of IPA. The mixture was subjected to ultrasonication for 14 h in an ice-bath followed by centrifugation at 500 rpm for 5 min to remove the poorly exfoliated antimony aggregates [31,32]. The two-thirds of the supernatant was pipetted out and subsequently filtered and dried in the air overnight.

## *2.3. Synthesis of Sb<sub>2</sub>O<sub>3</sub> modified W<sub>18</sub>O<sub>49</sub> (Sb<sub>2</sub>O<sub>3</sub>/W<sub>18</sub>O<sub>49</sub>) photocatalysts*

Sb<sub>2</sub>O<sub>3</sub>/W<sub>18</sub>O<sub>49</sub> was prepared via a facile solvothermal method. Typically, to prepare Sb<sub>2</sub>O<sub>3</sub>/W<sub>18</sub>O<sub>49</sub> containing 18% weight percentage of Sb<sub>2</sub>O<sub>3</sub> (18% Sb<sub>2</sub>O<sub>3</sub>/W<sub>18</sub>O<sub>49</sub>), 10.24 mg of Sb nanosheets were added into 60 mL of absolute ethanol. The mixture was ultrasonicated for 30 min to form a uniform dispersion. Then 100 mg of WCl<sub>6</sub> was dissolved in the above suspension under vigorous magnetic stirring for 0.5 h. Subsequently, the mixture was loaded into a Teflon-lined autoclave and heated at 180 °C for 20 h, followed by naturally cooling to room temperature. Finally, the resultant precipitate was washed thoroughly with ethanol, deionized water, and ethanol in turn several times to remove ions and possible remnants, then dried at 60 °C in a vacuum oven overnight prior to use and characterization. A series of Sb<sub>2</sub>O<sub>3</sub>/W<sub>18</sub>O<sub>49</sub> composites with different Sb<sub>2</sub>O<sub>3</sub> weight loadings (e.g. 1.8%, 3%, 6%, 12%, 18%, 28%, 54%, and 70%) were synthesized by changing the adding amount of 2D Sb while keeping the other conditions

constant. As a control, bare  $\text{W}_{18}\text{O}_{49}$  was prepared according to the previously reported method without any further modification [20].

#### 2.4. Characterization

Powder X-ray diffraction (XRD) measurements were performed under  $\text{Cu K}\alpha$  radiation using a D/MAXRC diffractometer operated at 30 kV and 100 mA with a  $2\theta$  scan rate of  $5^\circ \text{ min}^{-1}$ . Diffraction patterns were taken over the  $2\theta$  range of  $20\text{--}80^\circ$ . Raman spectra were collected using a Renishaw in Via Raman microscope with an He/Ne laser excitation at 532 nm (2.33 eV). X-ray photoelectron spectroscopy (XPS) and valence band (VB) XPS experiments were conducted using a Thermo Scientific ESCALAB 250Xi instrument with an electron flood and scanning ion gun. The C 1s binding energy at 284.8 eV was used to correct the charge effects. The UV-vis diffuse-reflectance spectra (DRS) were measured using a Persee UV-vis spectroscopy (TU-1950) recorded over a 200–800 nm range with  $\text{BaSO}_4$  as the background. The photoluminescence (PL) spectra were acquired on a Hitachi F-7000 fluorescence spectrophotometer with an excitation wavelength of 350 nm. The sample cell used in the experiment is a four-sided transparent quartz cell, in which the samples are ultrasonically dispersed in ethanol to make suspensions of the same concentration. Transmission electron microscopy (TEM) and high-angle annular dark-field scanning TEM (HAADF-STEM) were carried out using a JEOL ARM200 microscope with 200 kV accelerating voltage. (S)TEM samples were prepared by depositing a droplet of sample suspension in ethanol onto a Cu grid coated with a lacey carbon film. Electron spin resonance (ESR) spectra were obtained using a Bruker escan ESR spectrometer ( $27^\circ \text{C}$ , 9.7397 GHz). The weight percentages of elements in the optimal photocatalyst were investigated by



inductively coupled plasma-atomic emission spectrometry (ICP-AES). Nitrogen temperature programmed desorption (N<sub>2</sub>-TPD) measurements were performed on the Autosorb-iQ apparatus.

### 2.5. *Electrochemical measurements*

The electrochemical analysis was performed on a CHI 660D electrochemical workstation (Shanghai Chenhua, China) at ambient conditions using a standard three-electrode quartz cell with Pt wire and Ag/AgCl electrode as counter and reference electrodes, respectively. To prepare a working electrode, 2 mg of the as-prepared catalyst powder was uniformly dropcast onto a 1 × 2 cm<sup>2</sup> fluorine-doped tin oxide (FTO) substrate by Nafion coating. In brief, samples was dispersed in 200 μL of IPA/H<sub>2</sub>O solution (volume ratio of 1:1) and 2 μL of 5% Nafion solution to form a homogeneous slurry by ultrasonication for at least 60 min. Subsequently, the catalyst ink was pipetted onto the FTO glass. After evaporation of IPA and water, the catalyst-coated FTO substrate was used as a working electrode. The electrolyte of 0.5 M Na<sub>2</sub>SO<sub>4</sub> aqueous solution was saturated in Ar for 30 min prior to further measurements at a frequency of 1 kHz. During electrochemical impedance measurements and photocurrent tests, the electrolyte was bubbled with Ar. The light source of the electrochemical photocurrent response tests (i.e. *I-t*) is a xenon lamp (MerryChange MC-X301), and the illumination time interval is 20 s (light on/off cycles: 20 s).

### 2.6. *Photocatalytic tests*

Photocatalytic N<sub>2</sub> fixation was carried out in a closed stainless reactor (50 mL) with a top quartz window for light irradiation. In a typical photocatalytic test,

photocatalysts (5 mg) were dispersed in the aqueous solution (10 mL) containing 20 vol% methanol (as a photogenerated hole scavenger), then were transferred into glassware in the reactor and sealed. Before executing the photocatalytic experiment, the reactor was evacuated by a pump and purged with high purity N<sub>2</sub> three times, each lasting 1 min, to remove air thoroughly from the system. Finally, N<sub>2</sub> with the pressure of 0.3 MPa was filled into the reactor. The reactor was irradiated with continuing stirring under simulated visible light (with a cut off filter,  $\lambda \geq 420$  nm) using a 300 W xenon lamp (PLS-SXE300, Beijing Perfect Light Technology Co., Ltd. China). The photoreactor was equipped with cooling water circulation system in order to ensure that the reaction is carried out at room temperature. The distance between reaction equipment and light was held at 6 cm. After 1 h of irradiation, the gas was discharged by bubbling into an offgas absorber containing 15 mL of 0.1 M HCl solution.

During the photocatalytic N<sub>2</sub> fixation reaction, the light resource was placed 11 cm away from reaction solution surface. The intensity of light at wavelength between 420 and 780 nm irradiation was measured to be 1200 mW cm<sup>-2</sup> by an FZ-A irradiance meter.

## 2.7. Density functional theory (DFT) calculations

All the DFT calculations are performed using the Vienna Ab Initio Simulation Package (VASP). The exchange-correlation potential is described by the generalized gradient approximation (GGA) with spin polarized Perdew–Burke–Ernzerhof (PBE) functional. The projector augmented wave is applied to describe the electron-ion interaction and the plane-wave energy cutoff is set to 400 eV. All structures are optimized with a convergence criterion of  $1 \times 10^{-5}$  eV for the energy

and 0.01 eV/Å for the forces. The vacuum spacing is set to more than 15 Å for surface isolation to prevent interaction between two neighboring surfaces. Brillouin zone sampling is employed using a Monkhorst-Packing grid with  $3 \times 3 \times 1$  for the calculated models. Denser k-points ( $3 \times 3 \times 1$ ) are used for the calculations of density of states (DOS).

### 3. Results and discussion

#### 3.1. Microstructure and morphology analysis

As illustrated in Fig. 1a,  $\text{Sb}_2\text{O}_3/\text{W}_{18}\text{O}_{49}$  heterostructures were facilely synthesized by liquid exfoliation of bulk Sb followed by a solvothermal process. The crystal structure of the prepared sample was first characterized by XRD (Fig. 1b). It can be seen that the exfoliated Sb nanosheets maintained high crystallinity [31]. The distinct diffraction peaks of (010), (014), (110), (202), and (024) planes are ascribed to typical hexagonal  $\beta$ -Sb nanocrystal (JCPDS no.: 35–0732) [32]. Relatively weak diffractions from  $\text{Sb}_2\text{O}_3$  (JCPDS no. 05–0534) were also observed due to oxidation of surface during exfoliation and exposure in the air [33]. Note that the (003) and (006) reflections located at 23.5 and 25.1 ° were dramatically weakened for 2D Sb relative to its bulk counterpart, suggesting the occurrence of delamination along the *c*-axis to form nanosheets. The reflection at 28.3 ° can be assigned to cubic  $\text{Sb}_2\text{O}_3$ , indicative of conversion of Sb to  $\text{Sb}_2\text{O}_3$  during the synthesis. For both pristine  $\text{W}_{18}\text{O}_{49}$  and  $\text{Sb}_2\text{O}_3/\text{W}_{18}\text{O}_{49}$ , the major diffraction peaks at  $2\theta = 23.2$  and 47.3 ° match well with the respective (010) and (020) facets of monoclinic  $\text{W}_{18}\text{O}_{49}$  (JCPDS no.: 71–2450). The strongest intensity of the (010) diffraction peak indicates that the metal oxide preferably grew along the [010] orientation. The (010) reflection of the composite slightly shifted toward a higher

$2\theta$  (Fig. S1), which may be a result of lattice mismatch due to surface decoration or introduction of interstitial heteroatoms. Owing to the equivalent radius between  $\text{Sb}^{5+}$  (0.62 Å) and  $\text{W}^{6+}$  (0.62 Å), it is probable that Sb ions may also dope into the  $\text{W}_{18}\text{O}_{49}$  structure by substituting  $\text{W}^{6+}$  ions to generate structural defects as active sites.

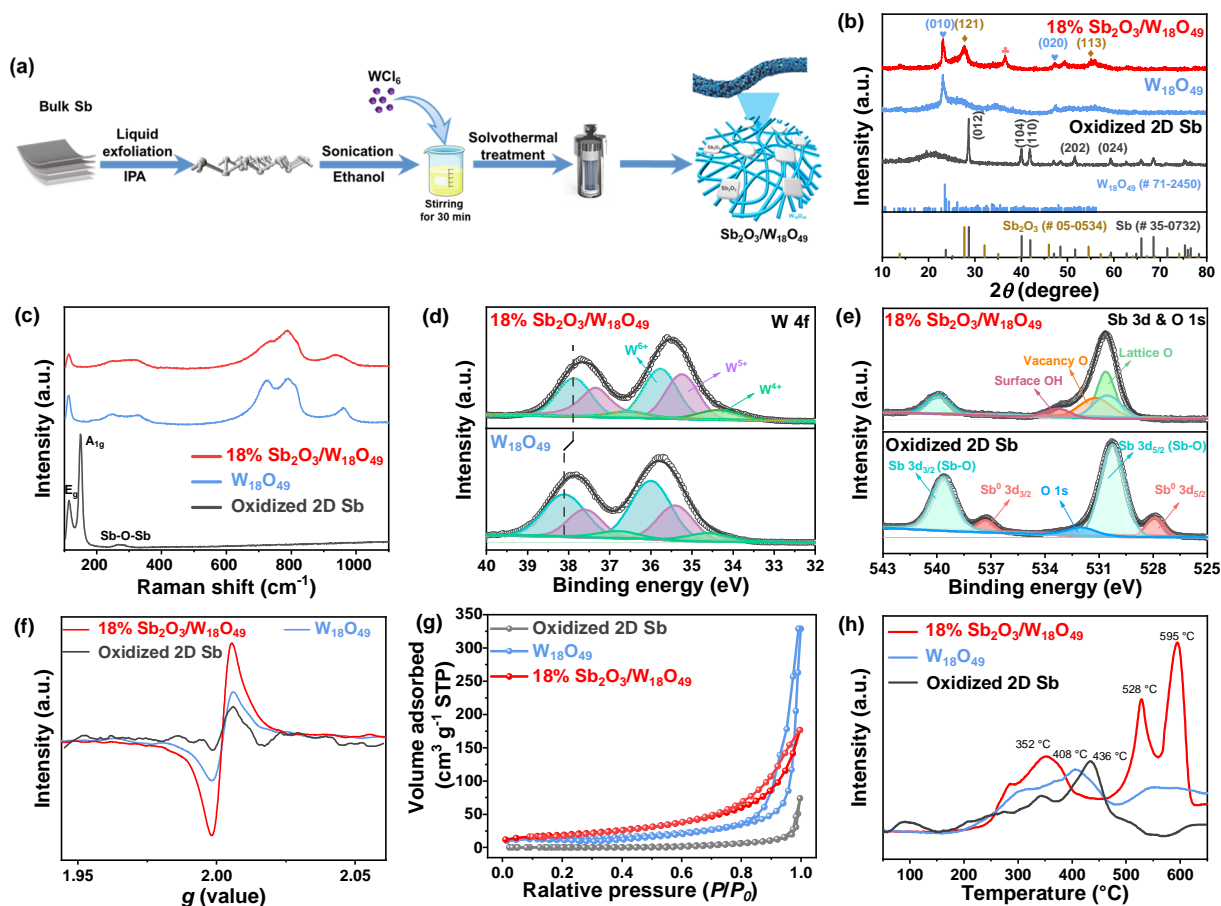


**Fig. 1.** (a) Schematic illustration of synthesis of  $\text{Sb}_2\text{O}_3/\text{W}_{18}\text{O}_{49}$  heterostructure. (b) XRD patterns and (c) Raman spectra of  $\text{W}_{18}\text{O}_{49}$ , 18%  $\text{Sb}_2\text{O}_3/\text{W}_{18}\text{O}_{49}$ , and oxidized 2D Sb. (d) W 4f XPS spectra of  $\text{W}_{18}\text{O}_{49}$  and 18%  $\text{Sb}_2\text{O}_3/\text{W}_{18}\text{O}_{49}$ . (e) Deconvoluted Sb 3d and O 1s XPS spectra of 18%  $\text{Sb}_2\text{O}_3/\text{W}_{18}\text{O}_{49}$  and oxidized 2D Sb. (f) ESR spectra, (g)  $\text{N}_2$  adsorption/desorption isotherms, and (h)  $\text{N}_2$ -TPD profiles of  $\text{W}_{18}\text{O}_{49}$ , 18%  $\text{Sb}_2\text{O}_3/\text{W}_{18}\text{O}_{49}$ , and oxidized 2D Sb.

Raman spectroscopy was used to investigate the local atomic arrangements

and vibrations of a crystal structure, which is considered to be a powerful tool for distinguishing the different phases of tungsten oxides, especially for tungsten suboxides. Although some reduced  $\text{WO}_{3-x}$  phases are also Raman active, they exhibit quite different Raman signals from those of  $\text{W}_{18}\text{O}_{49}$  [34]. As depicted in Fig. 1c, two sharp characteristic peaks centered at 115 and 149  $\text{cm}^{-1}$  were observed for oxidized Sb nanosheets, belonging to the in-plane vibrational  $E_g$  mode and the out-of-plane  $A_{1g}$  mode of 2D Sb, respectively [32]. The band at 260  $\text{cm}^{-1}$  can be attributed to the Sb–O–Sb stretching mode of  $\text{Sb}_2\text{O}_3$ . The antimony oxide likely resulted from reaction of Sb with HCl obtained from reaction of  $\text{WCl}_6$  and ethanol [20], followed by subsequent reaction of  $\text{Sb}^{3+}$  with ethanol. For both  $\text{W}_{18}\text{O}_{49}$  and  $\text{Sb}_2\text{O}_3/\text{W}_{18}\text{O}_{49}$ , there exist broad bands appearing in the wavenumber regions of 150–400 nm and 600–1100 nm, which is in agreement with the general characteristics of  $\text{W}_{18}\text{O}_{49}$  [35]. The features at *ca.* 241 and 328  $\text{cm}^{-1}$  can be ascribed to the O–W–O bending modes while the peaks at *ca.* 723 and 790  $\text{cm}^{-1}$  are attributed to the W–O. The peak intensity at 723  $\text{cm}^{-1}$  for  $\text{Sb}_2\text{O}_3/\text{W}_{18}\text{O}_{49}$  became much diminished compared to that of pure  $\text{W}_{18}\text{O}_{49}$ . This may be due to weakening of W–O bonds via lattice relaxation (induced by oxygen vacancy defects). The band at 110  $\text{cm}^{-1}$  related to the W–O–W bending mode of  $\text{WO}_3$  is also distinct [35]. It is apparent that the peaks became broader in  $\text{Sb}_2\text{O}_3/\text{W}_{18}\text{O}_{49}$  than those of bare  $\text{W}_{18}\text{O}_{49}$  because of the reduction in the content of  $\text{W}_{18}\text{O}_{49}$  and the longer length of the Sb–O bond. Also, the creation of vacant oxygen and adsorption of water molecules at O–vacancy sites diminished the W–O bond strength and resulted in peak broadening [36]. Neither blueshifting nor redshifting occurred in the W–O–W bending, O–W–O bending, and W–O stretching vibration modes. Whereas a weak W=O terminal vibration stretching mode at *ca.* 938  $\text{cm}^{-1}$  was found to blueshift,

which may arise from large amounts of structural defects introduced during the solvothermal process.

XPS measurements were performed to probe the surface composition and surface state of the hybrid catalysts. The wide-scan XPS spectrum manifests the spectroscopic features of W, O, and Sb (Fig. S2). As illustrated in Fig. 1d, three spin-orbit doublets could be deconvoluted for pristine  $W_{18}O_{49}$  and  $Sb_2O_3/W_{18}O_{49}$ , with binding energies (BEs) of W 4f<sub>5/2</sub> at 37.9 eV and W 4f<sub>7/2</sub> at 35.8 eV attributed to  $W^{6+}$ , and also two doublet peaks with BEs at 37.4 and 35.5 eV assigned to  $W^{5+}$ , and BEs at 36.6 and 34.4 eV corresponding to  $W^{4+}$  [20]. It is worth noting that the BEs of all the W 4f peaks in the hybrid shifted markedly to lower values compared to those of  $W_{18}O_{49}$ , indicating transfer of electrons from Sb to  $W_{18}O_{49}$ . This suggests strong interactions between  $Sb_2O_3$  and  $W_{18}O_{49}$  in the composite, which is conducive to the adsorption and reduction of  $N_2$  molecules in the oxygen vacancy of  $WO_{3-x}$ . We also note that the fractions of reduced tungsten,  $W^{4+}$  and  $W^{5+}$ , increased after incorporation of Sb, which is likely associated with the creation of positively charged oxygen vacancies with accompanying charge-compensating electrons. Two antimony environments were noticed in the Sb 3d spectrum of oxidized Sb nanosheets (Fig. 1e), which can be deconvoluted into two main spin-orbit split doublets with a splitting of 9.4 eV. The O 1s peak centered at around 532 eV overlapped with the Sb 3d<sub>5/2</sub> peak [32]. The weak peaks displayed at 528 and 537.3 eV can be ascribed to the Sb 3d<sub>5/2</sub> and Sb 3d<sub>3/2</sub> of metallic Sb ( $Sb^0$ ). The two intense signals at 530.3 and 539.7 eV are assigned to the oxidized Sb (e.g.  $Sb_2O_3$ ) [32]. For  $Sb_2O_3/W_{18}O_{49}$ , the Sb 3d peaks from the Sb–O bond shifted to higher BEs accounting for electronic interactions. Whereas the signal for  $Sb^0$  disappeared, consistent with XRD and Raman observations. The O 1s XPS signals which

overlapped with the Sb 3d<sub>5/2</sub> peak can be resolved into three sub-bands at 530.6, 531.3, and 533.3 eV corresponding to lattice oxygen, vacancy oxygen, and the surface oxygen of –OH species [32]. The missing lattice oxygen leaves excessive electrons in the lattice that can be trapped by the neighboring metal atoms to form low-valence W species. The existence of rich oxygen defects in W<sub>18</sub>O<sub>49</sub> is expected to result in the strong tails for light absorption in visible and near-infrared regions in addition to the intrinsic light absorption below 450 nm.

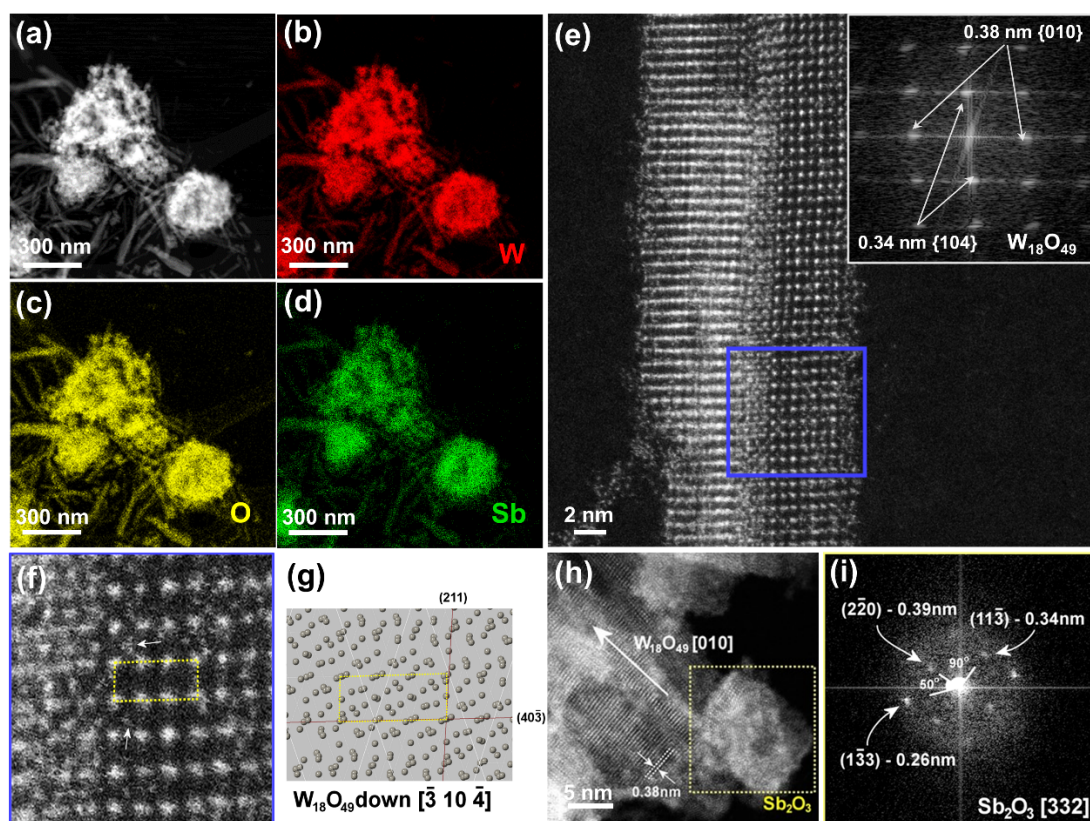
We further employed ESR spectroscopy to investigate the presence of oxygen vacancies in Sb<sub>2</sub>O<sub>3</sub>/W<sub>18</sub>O<sub>49</sub>. As revealed in Fig. 1f, resonance signals at  $g \approx 2.003$  with symmetric distributions were observed for W<sub>18</sub>O<sub>49</sub>, oxidized 2D Sb, and Sb<sub>2</sub>O<sub>3</sub>/W<sub>18</sub>O<sub>49</sub>, indicating the formation of abundant oxygen vacancies in the samples [26]. Evidently, the heterostructure exhibits drastically more intense ESR signals. This suggests generation of more unpaired electrons, which delocalize the lattice of W<sub>18</sub>O<sub>49</sub> providing more capture sites for photo-induced carriers to prevent their rapid recombination, thus promoting electron transfer to adsorbates during the photocatalytic process. The color change from pale blue (for pristine W<sub>18</sub>O<sub>49</sub>) to deep blue (for the heterostructure) also reflects the increase of oxygen vacancies (Fig. S3).

Fig. 1g depicts the N<sub>2</sub> adsorption-desorption isotherms of oxidized 2D Sb, W<sub>18</sub>O<sub>49</sub>, and Sb<sub>2</sub>O<sub>3</sub>/W<sub>18</sub>O<sub>49</sub>. A typical type I isotherm is observed according to the Brunauer–Deming–Deming–Teller classification, where the Brunauer–Emmett–Teller surface area of 18% Sb<sub>2</sub>O<sub>3</sub>/W<sub>18</sub>O<sub>49</sub> is 68.74 m<sup>2</sup> g<sup>−1</sup>, greater than that of oxidized Sb nanosheets and bare W<sub>18</sub>O<sub>49</sub>. N<sub>2</sub>-TPD profiles indicated that the as-made Sb<sub>2</sub>O<sub>3</sub>/W<sub>18</sub>O<sub>49</sub> exhibits outstanding N<sub>2</sub> uptake capacity (Fig. 1h). Pure W<sub>18</sub>O<sub>49</sub> displays a broad N<sub>2</sub> desorption peak at *ca.* 408 °C and oxidized 2D Sb

exhibits a main desorption peak at *ca.* 436 °C. In contrast, three sharper and stronger peaks centered at *ca.* 352, 528, and 595 °C were observed for Sb<sub>2</sub>O<sub>3</sub>/W<sub>18</sub>O<sub>49</sub>, attributed to desorption of chemisorbed N<sub>2</sub> from multiple active centers on the surface. The substantial enhancement in N<sub>2</sub> adsorption undoubtedly favors cleavage of the electron distribution symmetry, weakening the N≡N bond and increasing proton affinity to N<sub>2</sub>, benefiting its activation.

The morphology, microstructure, and composition of Sb<sub>2</sub>O<sub>3</sub>/W<sub>18</sub>O<sub>49</sub> were further examined by HAADF-STEM equipped with energy dispersive X-ray spectroscopy (EDS) (Fig. 2). A composite nanostructure comprising a large number of ultrathin nanowires of about 2 nm in diameter with length at a micrometre scale and flakes with sizes ranging from 15–300 nm were observed. Many nanowires oriented parallel to each other and formed bundles, probably due to van der Waals forces between neighboring nanowires. The large ratio of length to diameter provides high surface areas to expose more active sites, which is conducive to high catalytic activity. Elemental maps (Fig. 2b–d), along with the EDS spectrum (Fig. S4), clearly confirmed the prevalence of Sb, W, and O uniformly distributed on the surface of the hybrid. High-magnification STEM images (Fig. 2e, f, and h) and fast Fourier transforms (FFT) (inset of Fig. 2e and Fig. 2i) revealed a large contact interface between the two crystalline metal oxides. Almost all the surface of Sb<sub>2</sub>O<sub>3</sub> is covered by W<sub>18</sub>O<sub>49</sub>. The nanowires seem to grow along the [010] direction and possess good crystallinity with an interplanar spacing fringe of about 3.8 Å, ascribed to the (010) planes of monoclinic W<sub>18</sub>O<sub>49</sub>.





**Fig. 2.** (a) HAADF-STEM image of 18%  $\text{Sb}_2\text{O}_3/\text{W}_{18}\text{O}_{49}$  and corresponding EDS elemental maps of (b) W, (c) O, and (d) Sb elements. (e) High-magnification STEM image of 18%  $\text{Sb}_2\text{O}_3/\text{W}_{18}\text{O}_{49}$ . The inset shows its corresponding FFT pattern. (f) Enlarged STEM image of the region enclosed by the blue square in image e, and (g) corresponding reference structure for the main phase of  $\text{W}_{18}\text{O}_{49}$ . (h) STEM image and (i) respective FFT of the region enclosed by the yellow square in image h.

### 3.2. Photocatalytic property examination

The as-obtained  $\text{Sb}_2\text{O}_3/\text{W}_{18}\text{O}_{49}$  heterostructure composites with varying Sb loading levels were investigated for  $\text{N}_2$  fixation at about 25 °C without cocatalysts in  $\text{N}_2$ -saturated water using methanol as the hole scavenger under visible light illumination, as shown in Fig. S5. The concentration of produced  $\text{NH}_4^+$  in both the photoreaction suspension and the tail gas absorption solution was quantified using

the indophenol blue indicator method (Figs. S6 and S7) [37]. Shown in Fig. 3a are the photocatalytic results of oxidized 2D Sb,  $W_{18}O_{49}$ ,  $Sb_2O_3$ , and  $Sb_2O_3/W_{18}O_{49}$  samples with different Sb contents. It can be seen that both bare  $W_{18}O_{49}$  and oxidized Sb nanosheets exhibit low  $N_2$  reduction ability. To our delight, the construction of an  $Sb_2O_3/W_{18}O_{49}$  heterostructure substantially enhanced activities for  $N_2$  photofixation toward  $NH_3$ . No  $N_2H_4$  by-product was detected by the Watt and Chrisp method [38], indicating high selectivity for  $NH_3$  production (Figs. S8 and S9). Manipulation of the Sb loading level permits tuning of the  $NH_3$  generation rate. The  $Sb_2O_3/W_{18}O_{49}$  catalyst with an  $Sb_2O_3$  weight fraction of 18% delivered the largest average  $NH_3$  yield rate of  $600.1 \mu g_{NH_3} h^{-1} g_{cat.}^{-1}$  under visible light illumination, 3.4 and 5.5 times that of discrete  $W_{18}O_{49}$  and  $Sb_2O_3$ , respectively, and also noticeably outperforming mechanically mixed  $W_{18}O_{49}$  and Sb with equivalent Sb loadings (Fig. S10). The evolution rate of  $NH_3$  was also measured by ion chromatography, which was quantified to be about  $654 \mu g_{NH_3} h^{-1} g_{cat.}^{-1}$  (Fig. S11), plausibly matching the value estimated by the indophenol blue method. A production rate of  $NH_3$  was also detected to be  $660 \mu g_{NH_3} h^{-1} g_{cat.}^{-1}$  by ion selective electrode, as indicated in Fig. S12. The apparent quantum yield of the reaction was estimated to be *ca.* 0.063%. The turnover frequency (TOF) based on the overall mole of the  $Sb_2O_3/W_{18}O_{49}$  catalyst was determined to be  $0.05 h^{-1}$ . Notably, our catalyst exceeds many previously reported photocatalysts in terms of both  $NH_3$  yield rate and TOF (Table S1). Nonetheless, the  $NH_3$  production rate dropped upon further improving  $Sb_2O_3$  content beyond 18 wt%. This is likely due to agglomeration of  $Sb_2O_3$  and decrease in active interface areas of  $Sb_2O_3/W_{18}O_{49}$ , thus leading to weakened  $N_2$  adsorption and activation (as illustrated in the following DFT calculations).

To avoid false positives from background  $\text{NH}_3$  in the system or contamination from external sources, the photochemical  $\text{N}_2$  reduction was carried out with special care. Prior to NRR measurements, the  $\text{N}_2$  feeding gas (99.999% purity) was pre-purified to remove possible  $\text{NH}_3$  and labile nitrogen-containing contaminants (such as nitric oxides, nitrates or nitrites) (Fig. S13) [4,39]. Spectrophotometric tests confirmed that almost no  $\text{NO}_3^-$  and  $\text{NO}_2^-$  existed in the  $\text{N}_2$ -purged solution (Figs. S14–S16). To validate the origin of the produced  $\text{NH}_3$ , a series of blank and control experiments were performed. As illustrated in Figs. 3b, c and S6, marginal  $\text{NH}_3$  was detected in Ar (99.999% purity)-saturated solution, in the dark or in the absence of catalyst as a control. Meanwhile, almost no  $\text{NH}_3$  was detected in methanol solutions after being open in the air for 12 h (Fig. S17), thus eliminating the impact of possible contamination from the air. The effect of operator breath was also ruled out by the result that negligible  $\text{NH}_4^+$  was probed after leaving the solution close to the operator for 1 h (Fig. S17). To investigate if minor amounts of impurities in  $\text{N}_2$  (99.999%) may influence the photocatalytic results,  $\text{N}_2$  (99.9999%, Fig. S17) with higher purity was applied as a feed gas. Similar  $\text{NH}_3$  production rates were obtained (Fig. S17). The  $\text{N}_2$  (99.9999%) was further cleaned by adsorption using 10 M NaOH solution or alternatively with 1 M  $\text{NaClO}_2$  solution and subsequently with 10 M NaOH solution to exclude  $\text{NO}_x$  in the feed gas. Nearly equivalent  $\text{NH}_3$  yield rates were attained (Fig. S17). Among others, no nitrogen-containing chemicals were involved during preparation of  $\text{Sb}_2\text{O}_3/\text{W}_{18}\text{O}_{49}$ , thus ruling out possible interferences from the catalysts. This can be confirmed by XPS survey (Fig. S2), from which no obvious BE peak of N species can be identified. These combined results imply that  $\text{NH}_3$  evolved from the reduction of dissolved  $\text{N}_2$  catalyzed by  $\text{Sb}_2\text{O}_3/\text{W}_{18}\text{O}_{49}$ .

Continuous  $\text{NH}_3$  production was attained on the  $\text{Sb}_2\text{O}_3/\text{W}_{18}\text{O}_{49}$  catalyst and a

quasi-linear correlation between  $\text{NH}_3$  yield and irradiation time was observed during the reaction period of 3 hours (Fig. 3b). Post characterization by XRD (Fig. S18) and TEM (Fig. S19) showed that the crystalline structure of the composite was preserved after the NRR. The heterostructures also exhibited good repeatability with nearly constant  $\text{NH}_3$  yield rates by use of 10 different batches of  $\text{Sb}_2\text{O}_3/\text{W}_{18}\text{O}_{49}$  samples (Fig. 3c). Moreover, cycling tests revealed that the catalytic activity was largely retained even after five successive cycles (Fig. 3d). The certain loss of activity may result from aggregation of  $\text{Sb}_2\text{O}_3/\text{W}_{18}\text{O}_{49}$  sample. Overall, these indicates good stability and reproducibility of the photocatalytic performance.

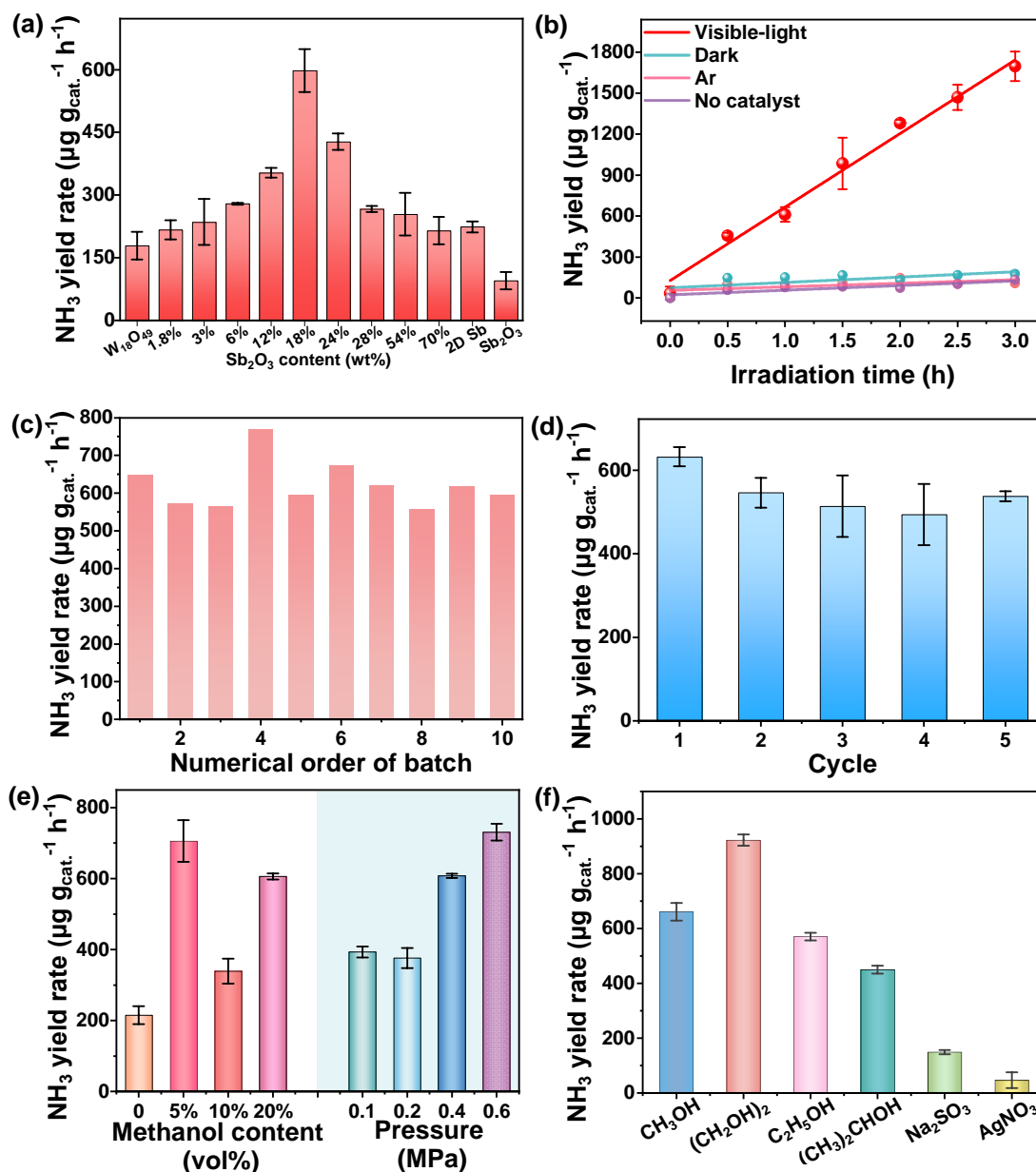


**Fig. 3.** (a)  $\text{NH}_3$  yield rate acquired under visible light irradiation over neat  $\text{W}_{18}\text{O}_{49}$ , oxidized 2D Sb,  $\text{Sb}_2\text{O}_3$ , and  $\text{Sb}_2\text{O}_3/\text{W}_{18}\text{O}_{49}$  samples with different Sb loading percentages. (b)  $\text{NH}_3$  yield as a function of irradiation time over 18%  $\text{Sb}_2\text{O}_3/\text{W}_{18}\text{O}_{49}$  in the dark (Dark), Ar atmosphere (Ar) (by visible light illumination), visible light, or without catalysts (No catalyst). (c) The  $\text{NH}_3$  yield rates over 10 different batches of  $\text{Sb}_2\text{O}_3/\text{W}_{18}\text{O}_{49}$  samples. (d)  $\text{NH}_3$  yield rate of 18%  $\text{Sb}_2\text{O}_3/\text{W}_{18}\text{O}_{49}$  against recycling cycle. (e)  $\text{NH}_3$  yield rate of 18%  $\text{Sb}_2\text{O}_3/\text{W}_{18}\text{O}_{49}$  versus methanol content (left panel) and  $\text{N}_2$  pressure (right panel). (f)  $\text{NH}_3$  yield rates of 18%  $\text{Sb}_2\text{O}_3/\text{W}_{18}\text{O}_{49}$

in 20 vol% aqueous solutions of methanol, ethylene glycol, ethanol, isopropanol, 1mM Na<sub>2</sub>SO<sub>3</sub> solution, or AgNO<sub>3</sub> trapping agents.

We also studied the influence of methanol concentration and feed gas pressure on the yield of NH<sub>3</sub>. As shown in Fig. 3f, the optimal N<sub>2</sub> reduction activity is 731  $\mu\text{g}_{\text{NH}_3} \text{ h}^{-1} \text{ g}_{\text{cat.}}^{-1}$  at 5 vol% of methanol and 0.6 MPa of N<sub>2</sub>. Elevating N<sub>2</sub> pressure tended to augment N<sub>2</sub> solubility and diffusivity [4], thereby promoting the NRR. In pure water, dramatically decreased activity was observed, indicating that the sacrificial electron donors play an important role in capturing photogenerated holes, thus favoring NH<sub>3</sub> production. A certain amount of methanol (i.e. 5 vol%) can facilitate water oxidation by consuming  $\cdot\text{OH}$  generated from H<sub>2</sub>O, hence boosting charge-carrier separation and improving the photoreduction efficiency [32]. While further addition of the trapping agent over 10 vol% may lead to preferential adsorption of methanol, inhibiting the adsorption of H<sub>2</sub>O and consequently suppressing the NRR. When further improving the methanol concentration (20 vol%), the ammonia production started to increase; this can be explained by the possibility that the decreased photogenerated electrons to the conduction band (CB) is compensated by the increased hole transfer to methanol since the hole oxidation of methanol is easier. We also investigated the effect of a variety of trapping agents concerning photocatalytic NH<sub>3</sub> production over Sb<sub>2</sub>O<sub>3</sub>/W<sub>18</sub>O<sub>49</sub> photocatalysts in 20 vol% alcohol–water or 1 mM Na<sub>2</sub>SO<sub>3</sub> systems, given that their properties can considerably affect the electron transfer kinetics. Photocatalytic NH<sub>3</sub> production strongly depends on the sacrificial hole scavenger, with the rate decreasing in the order of ethylene glycol > methanol > ethanol > isopropanol > Na<sub>2</sub>SO<sub>3</sub>. Ethylene glycol afforded the highest NH<sub>3</sub> yield rates, which is probably owing to its lowest

oxidation potential and higher alcohol polarizability (Table S2) [40], making it the best sacrificial hole scavenger. In the presence of  $\text{AgNO}_3$  used as an electron scavenger, the  $\text{NH}_3$  production is heavily hampered, implying that photogenerated electrons are crucial to triggering the reduction reaction.

Solid UV-vis diffused reflectance spectroscopy (UV-DRS) analysis (Fig. 4a) showed that  $\text{Sb}_2\text{O}_3/\text{W}_{18}\text{O}_{49}$ ,  $\text{W}_{18}\text{O}_{49}$ , and oxidized Sb nanosheets all exhibit a broad light response in the range from 300 to 800 nm, indicating their good visible light absorption capacities, likely a result of the coherent oscillations of surface free electrons caused by the presence of abundant oxygen vacancies [41]. In particular,  $\text{Sb}_2\text{O}_3/\text{W}_{18}\text{O}_{49}$  and  $\text{W}_{18}\text{O}_{49}$  possess a strong valence-to-conduction band transition absorption, with an absorption band edge at 570 and 470 nm, respectively. The notable redshift of the absorption edges demonstrated that the incorporation of ultrathin  $\text{Sb}_2\text{O}_3$  nanosheets reduced the bandgap of  $\text{W}_{18}\text{O}_{49}$ .

Photoluminescence (PL) spectroscopy showed a prominent emission peak centered at about 700 nm (Fig. 4b), which is related to the radiative recombination of carriers or excitons [42,43]. Strikingly, the 18%  $\text{Sb}_2\text{O}_3/\text{W}_{18}\text{O}_{49}$  provided the weakest emission, indicative of its lowest charge recombination rate. Time-resolved photoluminescence (TRPL) spectroscopy was conducted to further explore the charge movement dynamics. The decay curves of the three samples were fitted by two-exponential kinetics function (Fig. 4c). We found that the average fluorescence lifetime of 18%  $\text{Sb}_2\text{O}_3/\text{W}_{18}\text{O}_{49}$  (3.66 ns) is longer than that of pristine  $\text{W}_{18}\text{O}_{49}$  (1.68 ns) and oxidized Sb nanosheets (1.16 ns), meaning that the integration of  $\text{W}_{18}\text{O}_{49}$  with  $\text{Sb}_2\text{O}_3$  facilitated a more effective nonradiative decay pathway, therefore enabling easy transfer of photogenerated electrons to the catalyst surface rather than recombination with holes during migration.



As presented in Fig. 4d, the transient photocurrent responses of the samples with several on-off cycles of intermittent irradiation were found to be very stable and reversible. Especially, the  $\text{Sb}_2\text{O}_3/\text{W}_{18}\text{O}_{49}$  gave a remarkably higher photocurrent density as compared with  $\text{W}_{18}\text{O}_{49}$  and oxidized 2D Sb in accord with the PL spectra, suggesting enhanced photogenerated charge migration in the composite [44,45]. Fig. 4e displays the linear sweep voltammetry (LSV) curves of oxidized Sb nanosheets,  $\text{W}_{18}\text{O}_{49}$ , and  $\text{Sb}_2\text{O}_3/\text{W}_{18}\text{O}_{49}$  in  $\text{N}_2$  ( $\geq 99.999\%$ ) and Ar ( $\geq 99.999\%$ ) saturated electrolytes. It is noteworthy that  $\text{Sb}_2\text{O}_3/\text{W}_{18}\text{O}_{49}$  presented a considerably higher reductive current density than pure  $\text{W}_{18}\text{O}_{49}$  and oxidized 2D Sb, suggesting its superior capability for NRR. Electrochemical impedance spectroscopy (EIS) measurements (Fig. 4f) showed that  $\text{Sb}_2\text{O}_3/\text{W}_{18}\text{O}_{49}$  had the smallest charge transfer resistance ( $R_{\text{ct}}$ ) [46,47]. As a consequence, more photo-induced carriers can participate in redox reactions per unit time, thereby enhancing photocatalytic efficiency.

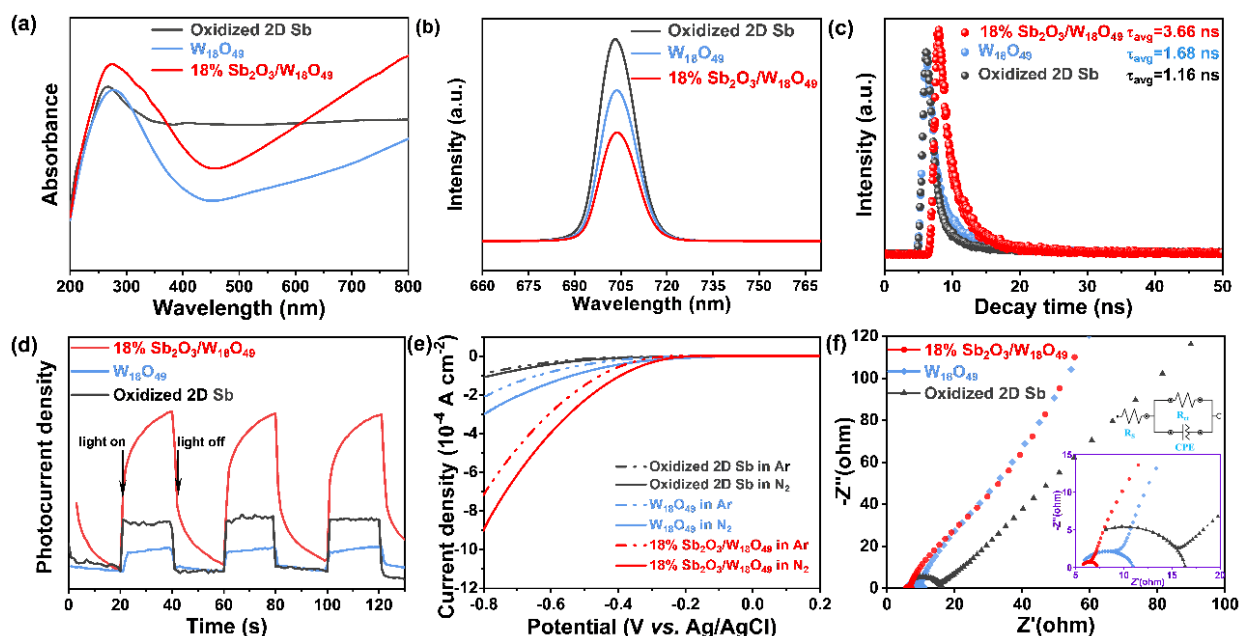


**Fig. 4.** (a) UV-vis diffuse-reflectance absorption spectra, (b) steady-state PL profiles, (c) time-resolved PL spectra, (d) photocurrent responses, (e) LSV curves



in Ar- (dashed line) or N<sub>2</sub>- (solid line) saturated electrolyte, and (f) Nyquist plots of 18% Sb<sub>2</sub>O<sub>3</sub>/W<sub>18</sub>O<sub>49</sub>, W<sub>18</sub>O<sub>49</sub>, and oxidized 2D Sb. The top inset is the equivalent circuit used for fitting the data, where  $R_s$  represents the combination of the resistance of electrodes and electrolyte, CPE and  $R_{ct}$  stand for the capacitance and charge transfer resistance of working electrode-electrolyte interface, respectively. The bottom inset is the enlarged EIS profile.

Based on UV-DRS data, the bandgap energies of Sb<sub>2</sub>O<sub>3</sub>/W<sub>18</sub>O<sub>49</sub>, W<sub>18</sub>O<sub>49</sub>, and oxidized Sb nanosheets were calculated by the Kubelka-Munk function. The optical bandgaps ( $E_g$ ) were deduced by the following Tauc plot:  $\alpha h\nu = A(h\nu - E_g)^n$ , where  $\alpha$  is the absorption coefficient,  $h$  is Planck's constant,  $\nu$  is the photon frequency, and  $A$  is the parameter that hinges on transmission probability. Here,  $n$  is 2 with respect to direct allowed transitions [4,48]. The intercepts were obtained by extrapolating the straightest line part of  $(\alpha h\nu)^{1/n}$  versus  $(h\nu)$  plot to the  $x$ -axis ( $h\nu$ ) to estimate the bandgaps. As denoted in Fig. 5a, The  $E_g$  values of oxidized Sb nanosheets, W<sub>18</sub>O<sub>49</sub>, and 18% Sb<sub>2</sub>O<sub>3</sub>/W<sub>18</sub>O<sub>49</sub> were determined to be 2.75, 2.95, and 2.85 eV, respectively. Furthermore, Mott-Schottky electrochemical measurements at a frequency of 1 kHz were implemented to confirm the type of a semiconductor and its flat band potential position ( $E_{fb}$ ). It is well recognized that the flat charge potential of an  $n$ -type semiconductor is close to the CB edge. The value of the CB can thus be estimated via the Mott-Schottky plot. Fig. 5b presents the Mott-Schottky plots,  $1/C^2$  as a function of electrochemical potential, where the capacitance  $C$  was obtained from the impedance measurements. The positive slopes of the linear parts verified the  $n$ -type nature of all the prepared samples. Moreover, from the intercepts of the extrapolated lines, the  $E_{fb}$  values of oxidized 2D Sb, W<sub>18</sub>O<sub>49</sub>, and 18% Sb<sub>2</sub>O<sub>3</sub>/W<sub>18</sub>O<sub>49</sub> were derived to be -0.37, -0.33, and -0.35 V (vs. Ag/AgCl),

corresponding to  $-0.173$ ,  $-0.133$ , and  $-0.153$  V (vs. NHE, pH 0), respectively. Generally, the bottom of CB potential is more negative by  $\sim -0.1$  V than the  $E_{fb}$  for *n*-type semiconductors [49]. Therefore, the respective  $E_{CB}$  of oxidized 2D Sb,  $W_{18}O_{49}$ , and 18%  $Sb_2O_3/W_{18}O_{49}$  were inferred to be about  $-0.073$ ,  $-0.033$ , and  $-0.053$  V (vs. NHE, pH 0). The corresponding valence band energy  $E_{VB}$  is thus calculated from  $E_{CB}$  plus bandgap width, which were 2.577, 2.917, and 2.797 V (vs. NHE, pH 0). It is evident that the reduction potential of the conduction band minimum (CBM) for  $Sb_2O_3/W_{18}O_{49}$  is located above that of  $N_2/NH_3$  ( $-0.05$  V vs. NHE, pH 0) [4], indicating that it is thermodynamically favorable for the heterojunction structures to trigger molecular  $N_2$  reduction. According to the VB XPS spectra (Fig. 5c), which reflects a band edge position relative to the Fermi level ( $E_F$ ), the valence band maximum (VBM) positions of oxidized 2D Sb,  $W_{18}O_{49}$ , and 18%  $Sb_2O_3/W_{18}O_{49}$  were measured to be 0.7, 2.3, and 1.8 eV below  $E_F$ , respectively, indicating the upshift of the VBM due to induced oxygen vacancies. According to the results of band gaps and band positions, the band structure diagrams are schematically provided in Fig. 5d.

According to energy band theory, the difference between the Fermi levels causes the electrons in  $W_{18}O_{49}$  with a higher  $E_F$  to flow into  $Sb_2O_3$  at the interface until the Fermi levels of the two components in the heterojunction are equal, which agrees well with the VB XPS result. Two charge transfer mechanisms are considered in the  $Sb_2O_3/W_{18}O_{49}$  heterostructures: the typical route (type II) and the Z-scheme. Given that the CB of  $W_{18}O_{49}$  is more positive than reduction potentials related to  $N_2$  to  $NH_3$ , type II structure cannot provide higher electron driving force. Alternatively, according to the above experimental results and analysis, the heterostructure composites are more likely to follow a Z-scheme charge transfer

route. The loaded  $\text{Sb}_2\text{O}_3$  can act as an electron trapper to prevent the recombination of photogenerated charge carriers. The exact mechanism of photocatalytic  $\text{N}_2$  reduction by the  $\text{Sb}_2\text{O}_3/\text{W}_{18}\text{O}_{49}$  remains elusive. It is most probable that electron–hole pairs were induced mainly in Sb under visible light irradiation (Fig. 6). Photoexcited electrons were rapidly transported to the CB of  $\text{Sb}_2\text{O}_3$  and also to  $\text{W}_{18}\text{O}_{49}$  through the interface to react with  $\text{N}_2$  to yield  $\text{NH}_3$ . Photogenerated holes were consumed by the methanol sacrificial agent. The oxygen vacancy-rich  $\text{W}_{18}\text{O}_{49}$  in the heterostructure favored adsorption and activation of  $\text{N}_2$  molecules. The low-valence Sb species may also polarize the chemisorbed  $\text{N}_2$  molecules and facilitate the electron transfer from coordinatively unsaturated sites to  $\text{N}_2$  adsorbates, making dissociation of the  $\text{N}\equiv\text{N}$  bond more feasible [29]. From these scenarios, we speculated that the active centers in the hybrids entail the oxygen vacancies in  $\text{W}_{18}\text{O}_{49}$  and also the edge sites of  $\text{Sb}_2\text{O}_3$  (i.e. exposed Sb atoms).

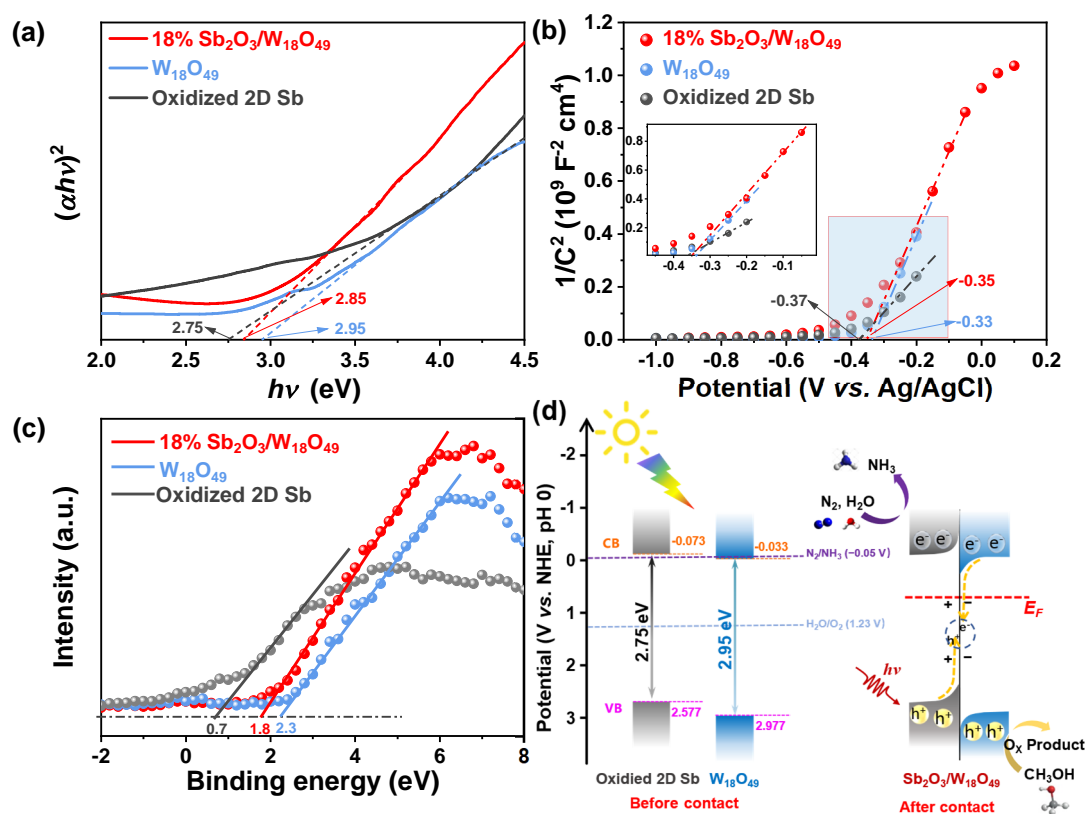


**Fig. 5.** (a) Tauc plots, (b) Mott-Schottky plots according to impedance measurements, and (c) VB XPS spectra, and (d) schematic diagrams of 18% Sb<sub>2</sub>O<sub>3</sub>/W<sub>18</sub>O<sub>49</sub>, W<sub>18</sub>O<sub>49</sub>, and oxidized 2D Sb.

### 3.3. DFT calculations

Further DFT calculations were carried out to investigate the adsorption and activation of N<sub>2</sub> on the surface of Sb<sub>2</sub>O<sub>3</sub>/W<sub>18</sub>O<sub>49</sub> and the catalytic mechanism of the NRR process. The Sb<sub>2</sub>O<sub>3</sub>/W<sub>18</sub>O<sub>49</sub> heterojunction model is adopted based on Sb<sub>2</sub>O<sub>3</sub> nanosheets supported on W<sub>18</sub>O<sub>49</sub> (010) surface, with the XRD and HAADF-STEM results being considered. Such exposed Sb<sub>2</sub>O<sub>3</sub> can dramatically improve the binding capability of the metal active sites in W<sub>18</sub>O<sub>49</sub> to N<sub>2</sub> molecules (Fig. 6 a). Before contact, only very small adsorption energies ( $\Delta E_{N_2^*}$ , relative to free N<sub>2</sub>) of  $-0.35$  to  $-0.45$  eV were achieved, which means N<sub>2</sub> molecules can only be very weakly adsorbed on their individual surfaces. Nevertheless, the  $\Delta E_{N_2^*}$  for the composite could be substantially enhanced to  $-1.08$  eV. DFT calculation revealed that the role of oxygen vacancies is to stabilize and tune the valence state of Sb atoms on the surface, and also to expose highly active metal atoms to adsorb nitrogen. This coincides with the above-mentioned N<sub>2</sub>-TPD result. According to the projected partial density of states (PDOS) (Fig. 6 b), the electron density on the Fermi level for Sb<sub>2</sub>O<sub>3</sub>/W<sub>18</sub>O<sub>49</sub> significantly increases, which can greatly promote N<sub>2</sub> reduction. After N<sub>2</sub> is adsorbed on the heterostructure, the total DOS of the catalyst is disturbed, with a large DOS change around  $-3$  eV, corresponding to the *d*-band or small *p*-orbital electrons. This demonstrates that the heterostructure tends to adsorb N<sub>2</sub> by hybridizing the triple bond of N<sub>2</sub> with *d*-band or *p*-orbital electrons. Deeper insights can be obtained from the differential charge density distributions

in the left-bottom inset of Fig. 6c. It illustrates that electron transfer of 0.25  $|e|$  occurs from Sb atoms to  $W_{18}O_{49}$ , forming an electrophilic and nucleophilic region near the interface, consistent with the XPS results. The Bader charge analysis further reveals a remarkable electron donation to  $*N_2$ , which accepts a total of 0.75 or 0.53  $|e|$  from interfacial Sb or W site, respectively. The oxygen vacancy defect states in  $W_{18}O_{49}$  offers the photogenerated electrons with strong reducibility to physically adsorbed  $*N_2$  and sharply lowers the  $\pi^*$  orbital of  $*N_2$  below the CB edge. Prominent Sb-to- $N_2$   $\pi$ -back donation is expected to strongly facilitate the cleavage of  $N\equiv N$ , greatly boosting NRR kinetics. Therefore, the interfacial metal sites on  $Sb_2O_3/W_{18}O_{49}$  function as the main active centers which possess a strong donating electron ability to the empty  $N_2$  antibonding orbitals to trigger the following  $NH_3$  synthesis.

The Gibbs free energy profile is applied to analyze the preferable NRR pathway for ammonia synthesis at the interfaces over  $Sb_2O_3/W_{18}O_{49}$  (Fig. 6c), which prefers to proceed via the distal pathway. Strikingly, the free energy of the initial  $N_2$  activation ( $*N_2$ ) is  $-0.35$  eV, confirming feasible activation of  $N_2$ , which leads to a very low energy barrier for the first protonation step. The subsequent  $NH_3$  desorption ( $*NNH_3 \rightarrow *N + NH_3$ ) step occurs with the largest energy barrier of (0.65 eV), which is the potential-determining step (PDS) in this reaction pathway. The high PDS barrier to release the first  $NH_3$  molecule results from the relatively strong interactions between the  $Sb_2O_3/W_{18}O_{49}$  heterostructures and  $NH_3$ , implying the synergistic interplay of  $Sb_2O_3$  and  $W_{18}O_{49}$ .

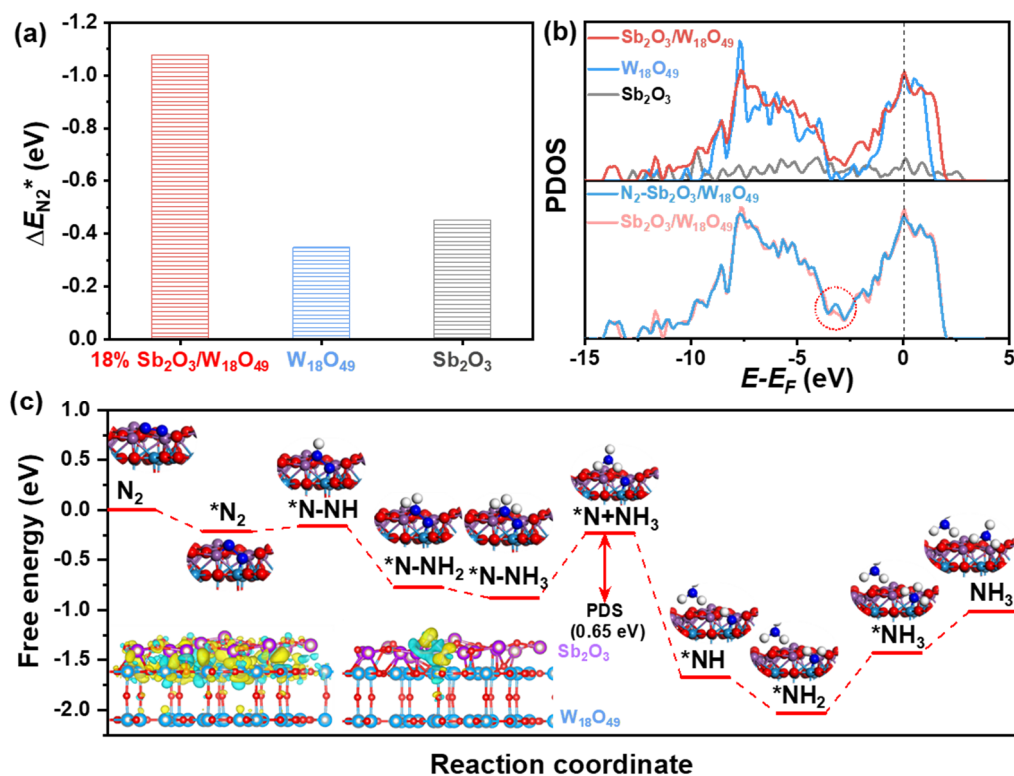


**Fig. 6.** (a) N<sub>2</sub> adsorption energy ( $\Delta E_{N_2^*}$ ) over Sb<sub>2</sub>O<sub>3</sub>, W<sub>18</sub>O<sub>49</sub>, 18% Sb<sub>2</sub>O<sub>3</sub>/W<sub>18</sub>O<sub>49</sub> by DFT calculations. (b) PDOSs of 18% Sb<sub>2</sub>O<sub>3</sub>/W<sub>18</sub>O<sub>49</sub> compared with before contact (top panel), and of \*N<sub>2</sub> over 18% Sb<sub>2</sub>O<sub>3</sub>/W<sub>18</sub>O<sub>49</sub> compared with that of counterparts. (c) Free energy profiles of the optimized NRR reaction pathway on Sb<sub>2</sub>O<sub>3</sub>/W<sub>18</sub>O<sub>49</sub>. The structures of reaction intermediates are shown next to their energy segments. The left bottom inset of (c) illustrates the differential charge density distributions at the interface between the heterojunction, and of N<sub>2</sub> chemisorbed on interfacial W-Sb sites, respectively. The yellow and cyan regions correspond to electron accumulation and electron depletion. The white, red, dark blue, light blue, and purple balls represent H, O, N, W, and Sb atoms, respectively.

#### 4. Conclusions

In summary, we show that construction of intimate interface between 2D Sb<sub>2</sub>O<sub>3</sub> and 1D W<sub>18</sub>O<sub>49</sub> nanowires could facilitate highly efficient photocatalytic N<sub>2</sub>

reduction to  $\text{NH}_3$  at ambient conditions. This hybrid catalyst afforded an average  $\text{NH}_3$  yield rate of  $600.1 \mu\text{g}_{\text{NH}_3} \text{h}^{-1} \text{g}_{\text{cat}}^{-1}$  under visible light illumination, 5.5 times and 3.4 times than that of neat  $\text{Sb}_2\text{O}_3$  and  $\text{W}_{18}\text{O}_{49}$ , and also outperforming many recently reported photocatalysts. The  $\text{NH}_3$  production rate can be further improved to  $731 \mu\text{g}_{\text{NH}_3} \text{h}^{-1} \text{g}_{\text{cat}}^{-1}$  by elevating the  $\text{N}_2$  pressure to 0.6 MPa. The photocatalytic performance retained good stability even after five successive reaction cycles. The superb catalytic activity was believed to originate from the cooperative impact of  $\text{Sb}_2\text{O}_3$  and  $\text{W}_{18}\text{O}_{49}$ . Their large interfacial contact greatly boosted charge-carrier migration and separation. In addition, the ultrafine nanowire structure with enlarged surface areas and abundant oxygen vacancies considerably increased the adsorption and activation of inert  $\text{N}_2$  molecules. The interfacial metal sites on  $\text{Sb}_2\text{O}_3/\text{W}_{18}\text{O}_{49}$  was proposed to be the major active centers to donate electrons to the empty  $\text{N}_2$  antibonding orbitals to trigger the subsequent reduction via the distal pathway. This work may shed light on the rational design of highly active materials for enhancing NRR and opens a path for solar energy harvesting from artificial photosynthesis by the use of robust and cost-effective photocatalysts.

#### **CRedit authorship contribution statement**

**X. Hui:** Data curation, Writing - original draft. **L. Li, S. Hong:** Data Curation, Visualization. **Q. Xia, L. Hao:** Review & editing. **A.W. Robertson:** Formal analysis, Visualization. **Z. Sun:** Conceptualization, Supervision, Funding acquisition, Writing.

#### **Declaration of competing interest**

The authors declare no conflicts of interest.

## Acknowledgments

This work was supported by the National Natural Science Foundation of China (No. 21972010); the Beijing Natural Science Foundation (No. 2192039); the Foundation of Key Laboratory of Low-Carbon Conversion Science & Engineering, Shanghai Advanced Research Institute, the Chinese Academy of Sciences (No. KLLCCSE-201901, SARI, CAS).

## Appendix A. Supplementary data

Supplementary data to this article can be found online at <https://doi.org/>

## References

- [1] Z. Liu, New design strategy of high efficiency catalysis system for ammonia synthesis at room temperature and atmospheric pressure, *Acta Phys. -Chim. Sin.* 35 (2019) 1171–1172.
- [2] Z. Zhao, J. Park, C. Choi, S. Hong, X. Hui, H. Zhang, T.W. Lo, A.W. Robertson, Z. Lv, Y. Jung, Z. Sun, Engineering vacancy and hydrophobicity of two-dimensional TaTe<sub>2</sub> for efficient and stable electrocatalytic N<sub>2</sub> reduction, *The Innovation* 3 (2022) 100190.
- [3] Y. Gao, H. Zhuo, Y. Cao, X. Sun, G. Zhuang, S. Deng, X. Zhong, Z. Wei, J. Wang, A theoretical study of electrocatalytic ammonia synthesis on single metal atom/MXene, *Chin. J. Catal.* 40 (2019) 152–159.
- [4] H. Shen, C. Choi, J. Masa, X. Li, J.S. Qiu, Y. Jung, Z. Sun, Electrochemical ammonia synthesis: mechanistic understanding and catalyst design, *Chem* 7 (2021) 1708–1754.



- [5] M. Zhang, C. Choi, R. Huo, G.H. Gu, S. Hong, C. Yan, S. Xu, A.W. Robertson, J. Qiu, Y. Jung, Z. Sun, Reduced graphene oxides with engineered defects enable efficient electrochemical reduction of dinitrogen to ammonia in wide pH range, *Nano Energy* 68 (2020) 104323.
- [6] Q. Liu, T. Xu, Y.L. Luo, Q.Q. Kong, T.S. Li, S.Y. Lu, A.A. Alshehri, K.A. Alzahrani, X.P. Sun, Recent advances in strategies for highly selective electrocatalytic N<sub>2</sub> reduction toward ambient NH<sub>3</sub> synthesis, *Curr. Opin. Electrochem.* 29 (2021) 100766.
- [7] Y. Shiraishi, M. Hashimoto, K. Chishiro, K. Moriyama, S. Tanaka, T. Hirai, Photocatalytic dinitrogen fixation with water on bismuth oxychloride in chloride solutions for solar-to-chemical energy conversion, *J. Am. Chem. Soc.* 142 (2020) 7574–7583.
- [8] H. Shen, M. Yang, L. Hao, J. Wang, J. Strunk, Z. Sun, Photocatalytic nitrogen reduction to ammonia: insights into the role of defect engineering in photocatalysts, *Nano Res.* 2022, DOI: 10.1007/s12274-021-3725-0.
- [9] G.N. Schrauzer, T.D. Guth, Photolysis of water and photoreduction of nitrogen on titanium dioxide, *J. Am. Chem. Soc.* 99 (1977) 7189–7193.
- [10] Z. Wang, J. Xu, H. Zhou, X. Zhang, Facile synthesis of Zn(II)-doped g-C<sub>3</sub>N<sub>4</sub> and their enhanced photocatalytic activity under visible light irradiation, *Rare Met.* 38 (2019) 459–467.
- [11] S. Liu, Y. Wang, S. Wang, M. You, S. Hong, T.-S. Wu, Y.-L. Soo, Z. Zhao, G. Jiang, J. Qiu, B. Wang, Z. Sun, Photocatalytic fixation of nitrogen to ammonia by single Ru atom decorated TiO<sub>2</sub> nanosheets, *ACS Sustainable Chem. Eng.* 7 (2019) 6813–6820.
- [12] Z. Zhao, S. Hong, C. Yan, C. Choi, Y.S. Jung, Y. Liu, S. Liu, X. Li, J. Qiu, Z.

Sun, Efficient visible-light driven N<sub>2</sub> fixation over two-dimensional Sb/TiO<sub>2</sub> composites, *Chem. Commun.* 55 (2019) 7171–7174.

[13] Z.R. Li, Z.Y. Ma, J. Liang, Y.C. Ren, T.S. Li, S.R. Xu, Q. Liu, N. Li, B. Tang, Y. Liu, S.Y. Gao, A.A. Alshehri, D.W. Ma, Y.L. Luo, Q. Wu, X.P. Sun, MnO<sub>2</sub> nanoarray with oxygen vacancies: An efficient catalyst for NO electroreduction to NH<sub>3</sub> at ambient conditions, *Mater. Today Phys.* 22 (2022) 100586.

[14] L.C. Zhang, J. Liang, Y.Y. Wang, T. Mou, Y.T. Lin, L.C. Yue, T.S. Li, Q. Liu, Y.L. Luo, N. Li, High-performance electrochemical NO reduction into NH<sub>3</sub> by MoS<sub>2</sub> nanosheet, *Angew. Chem. Int. Ed.* 133 (2021) 25467–25472.

[15] Q. Liu, L.S. Xie, J. Liang, Y.C. Ren, Y.Y. Wang, L.C. Zhang, L.C. Yue, T.S. Li, Y.S. Luo, N. Li, B. Tang, Y. Liu, S.Y. Gao, A.A. Alshehri, I. Shakir, P.O. Agboola, Q.Q. Kong, Q.Y. Wang, D.W. Ma, X.P. Sun, Ambient ammonia synthesis via electrochemical reduction of nitrate enabled by NiCo<sub>2</sub>O<sub>4</sub> nanowire array, *Small* (2022), 10.1002/sml.202106961.

[16] X.Z. Li, C.L. He, S.X. Zuo, X.Y. Yan, D. Dai, Y.Y. Zhang, C. Yao, Photocatalytic nitrogen fixation over fluoride/attapulgite nanocomposite: effect of upconversion and fluorine vacancy, *Sol. Energy* 191 (2019) 251–262.

[17] X.H. Ye, X.Z. Li, X.N. Chu, Z.D. Wang, S.X. Zuo, T.S. Wang, C. Yao, In situ construction of Fe substituted palygorskite/FeS<sub>2</sub> heterostructure for full-spectrum photocatalytic nitrogen fixation, *J. Alloys Compd.* 871 (2021) 159542.

[18] X.Z. Li, H.Y. Shi, S.X. Zuo, B.Y. Gao, C. Han, T.s. Wang, C. Yao, C.Y. Ni, Lattice reconstruction of one-dimensional mineral to achieve dendritic heterojunction for cost-effective nitrogen photofixation, *Chem. Eng. J.* 414 (2021) 128797.

[19] J.D. Liu, Z.X. Wei, Y.H. Dou, Y.Z. Feng, J.M. Ma, Ru-doped phosphorene for

electrochemical ammonia synthesis, *Rare Met.* 39 (2020) 874–880.

[20] M. Yang, R. Huo, H. Shen, Q. Xia, J. Qiu, A.W. Robertson, X. Li, Z. Sun, Metal-tuned  $W_{18}O_{49}$  for efficient electrocatalytic  $N_2$  reduction, *ACS Sustainable Chem. Eng.* 8 (2020) 2957–2963.

[21] S. Yin, Y. Asakura, Recent research progress on mixed valence state tungsten based materials, *Tungsten* 1 (2019) 5–18.

[22] Y. Tong, H. Guo, D. Liu, X. Yan, P. Su, J. Liang, S. Zhou, J. Liu, G.Q.M. Lu, S.X. Dou, Vacancy engineering of iron-doped  $W_{18}O_{49}$  nanoreactors for low-barrier electrochemical nitrogen reduction, *Angew. Chem. Int. Ed.* 59 (2020) 7356–7361.

[23] S. Cong, Y. Yuan, Z. Chen, J. Hou, M. Yang, Y. Su, Y. Zhang, L. Li, Q. Li, F. Geng, Z. Zhao, Noble metal-comparable SERS enhancement from semiconducting metal oxides by making oxygen vacancies, *Nat. Commun.* 6 (2015) 7800.

[24] Y.S. Fan, X.L. Xi, Y.S. Liu, Z.R. Nie, L.Y. Zhao, Q.H. Zhang, Regulation of morphology and visible light-driven photocatalysis of  $WO_3$  nanostructures by changing pH, *Rare Met.* 40 (2021) 1738–1745.

[25] Z. Sun, R. Huo, C. Choi, S. Hong, T.-S. Wu, J. Qiu, C. Yan, Z. Han, Y. Liu, Y.-L. Soo, Y. Jung, Oxygen vacancy enables electrochemical  $N_2$  fixation over  $WO_3$  with tailored structure, *Nano Energy* 62 (2019) 869–875.

[26] N. Zhang, A. Jalil, D. Wu, S. Chen, Y. Liu, C. Gao, W. Ye, Z. Qi, H. Ju, C. Wang, X. Wu, L. Song, J. Zhu, Y. Xiong, Refining defect states in  $W_{18}O_{49}$  by Mo doping: a strategy for tuning  $N_2$  activation towards solar-driven nitrogen fixation, *J. Am. Chem. Soc.* 140 (2018) 9434–9443.

[27] Z.B. Du, J. Liang, S.X. Li, Z.Q. Xu, T.S. Li, Q. Liu, Y.L. Luo, F. Zhang, Y. Liu, Q.Q. Kong, X.F. Shi, B. Tang, A.M. Asiri, B.H. Li, X.P. Sun, Alkylthiol surface engineering: an effective strategy toward enhanced electrocatalytic  $N_2$ -to- $NH_3$

- fixation by a CoP nanoarray, *J. Mater. Chem. A* 9 (2021) 13861–13866.
- [28] T. Xu, J. Liang, Y.Y. Wang, S.X. Li, Z.B. Du, T.S. Li, Q. Liu, Y.L. Luo, F. Zhang, X.F. Shi, B. Tang, Q.Q. Kong, A.M. Asiri, C. Yang, D.W. Ma, X.P. Sun, Enhancing electrocatalytic N<sub>2</sub>-to-NH<sub>3</sub> fixation by suppressing hydrogen evolution with alkylthiols modified Fe<sub>3</sub>P nanoarrays, *Nano Res.* 15 (2022) 1039–1046.
- [29] S.L. Zhang, Z. Yan, Y. Li, Z.F. Chen, H.B. Zeng, Atomically thin arsenene and antimonene: semimetal-semiconductor and indirect-direct band-gap transitions, *Angew. Chem.* 127 (2015) 3155–3158.
- [30] S.L. Zhang, M.Q. Xie, F.Y. Li, Z. Yan, Y.F. Li, E.J. Kan, W. Liu, Z.F. Chen, H.B. Zeng, Semiconducting group 15 monolayers: a broad range of band gaps and high carrier mobilities, *Angew. Chem.* 128 (2016) 1698–1701.
- [31] H. Tao, Y. Zhang, Y. Gao, Z. Sun, C. Yan, J. Texter, Scalable exfoliation and dispersion of two-dimensional materials—an update, *Phys. Chem. Chem. Phys.* 19 (2017) 921–960.
- [32] Z. Zhao, C. Choi, S. Hong, H. Shen, C. Yan, J. Masa, Y. Jung, J. Qiu, Z. Sun, Surface-engineered oxidized two-dimensional Sb for efficient visible light-driven N<sub>2</sub> fixation, *Nano Energy* 78 (2020) 105368.
- [33] X.H. Ren, Z.J. Li, H. Qiao, W.Y. Liang, H.T. Liu, F. Zhang, X. Qi, Y.D. Liu, Z.Y. Huang, D. Zhang, J.Q. Li, J.X. Zhong, H. Zhang, Few-layer Antimonene Nanosheet: a metal-free bifunctional electrocatalyst for effective water splitting, *ACS Appl. Energy Mater.* 2 (2019) 4774–4781.
- [34] D.Y. Lu, J. Chen, S.Z. Deng, N.S. Xu, W.H. Zhang, The most powerful tool for the structural analysis of tungsten suboxide nanowires: Raman spectroscopy, *J. Mater. Res.* 23 (2008) 402–408.
- [35] D.Y. Lu, J. Chen, J. Zhou, S.Z. Deng, N.S. Xu, J.B. Xu, Raman spectroscopic

study of oxidation and phase transition in  $\text{W}_{18}\text{O}_{49}$  nanowires, *J. Raman Spectrosc.* 38 (2007) 176–180.

[36] H. Zhang, Y. Wang, S. Zuo, W. Zhou, J. Zhang, X.W. Lou, Isolated cobalt centers on  $\text{W}_{18}\text{O}_{49}$  nanowires perform as a reaction switch for efficient  $\text{CO}_2$  photoreduction, *J. Am. Chem. Soc.* 143 (2021) 2173–2177.

[37] I. Ivančič, D. Degobbis, An optimal manual procedure for ammonia analysis in natural waters by the indophenol blue method. *Water Res.* 18 (1984) 1143–1147.

[38] G.W. Watt, J.D. Chrisp, Spectrophotometric method for determination of hydrazine, *Anal. Chem.* 24 (1952) 2006–2008.

[39] L. Yang, C. Choi, S. Hong, Z. Liu, Z. Zhao, M. Yang, H. Shen, A.W. Robertson, H. Zhang, T.W.B. Lo, Y. Jung, Z. Sun, Single yttrium sites on carbon-coated  $\text{TiO}_2$  for efficient electrocatalytic  $\text{N}_2$  reduction, *Chem. Commun.* 56 (2020) 10910–10913.

[40] W.T. Chen, A. Chan, Z.H.N. Al-Azri, A.G. Dosado, M.A. Nadeem, D. Sun-Waterhouse, H. Idriss, G.I.N. Waterhouse, Effect of  $\text{TiO}_2$  polymorph and alcohol sacrificial agent on the activity of  $\text{Au/TiO}_2$  photocatalysts for  $\text{H}_2$  production in alcohol-water mixtures, *J. Catal.* 329 (2015) 499–513.

[41] C.H. Shen, X.J. Wen, Z.H. Fei, Z.T. Liu, Q.M. Mu, Novel Z-scheme  $\text{W}_{18}\text{O}_{49}/\text{CeO}_2$  heterojunction for improved photocatalytic hydrogen evolution, *J. Colloid Interface Sci.* 579 (2020) 297–306.

[42] B.F. Li, W.J. Wang, J. Zhao, Z.Y. Wang, B. Su, Y.D. Hou, Z.X. Ding, W.J. Ong, S.B. Wang, All-solid-state direct Z-scheme  $\text{NiTiO}_3/\text{Cd}_{0.5}\text{Zn}_{0.5}\text{S}$  heterostructures for photocatalytic hydrogen evolution with visible light, *J. Mater. Chem. A* 9 (2021) 10270–10276.

[43] R.R. Wang, P.J. Yang, S.B. Wang, X. Wang, Distorted carbon nitride

nanosheets with activated  $n \rightarrow \pi^*$  transition and preferred textural properties for photocatalytic CO<sub>2</sub> reduction, *J. Catal.* 402 (2021) 166–176.

[44] H.M. Liu, P. Wu, H.T. Li, Z.B. Chen, L.Z. Wang, X. Zeng, Y.X. Zhu, Y.J. Jiang, X.Z. Liao, B.S. Haynes, J.H. Ye, C. Stampfl, J. Huang, Unravelling the effects of layered supports on Ru nanoparticles for enhancing N<sub>2</sub> reduction in photocatalytic ammonia synthesis, *Appl. Catal. B* 259 (2019) 118026.

[45] L.J. Huang, B.F. Li, B. Su, Z. Xiong, C.J. Zhang, Y.D. Hou, Z.X. Ding, S.B. Wang, Fabrication of hierarchical Co<sub>3</sub>O<sub>4</sub>@CdIn<sub>2</sub>S<sub>4</sub> p–n heterojunction photocatalysts for improved CO<sub>2</sub> reduction with visible light, *J. Mater. Chem. A* 8 (2020) 7177–7183.

[46] T.Y. Wang, C.T. Feng, J.Q. Liu, D.J. Wang, H.M. Hu, J. Hu, Z. Chen, G.L. Xue, Bi<sub>2</sub>WO<sub>6</sub> hollow microspheres with high specific surface area and oxygen vacancies for efficient photocatalysis N<sub>2</sub> fixation, *Chem. Eng. J.* 414 (2021) 128827.

[47] X.H. Lin, Z.D. Xie, B. Su, M. Zheng, W.X. Dai, Y.D. Hou, Z.X. Ding, W. Lin, Y.X. Fang, S.B. Wang, Well-defined Co<sub>9</sub>S<sub>8</sub> cages enable the separation of photoexcited charges to promote visible-light CO<sub>2</sub> reduction, *Nanoscale* 13 (2021) 18070–18076.

[48] D.R. Jones, V. Gomez, J.C. Bear, B. Rome, F. Mazzali, J.D. McGettrick, A.R. Lewis, S. Margadonna, W.A. Al-Masry, C.W. Dunnill, Active removal of waste dye pollutants using Ta<sub>3</sub>N<sub>5</sub>/W<sub>18</sub>O<sub>49</sub> nanocomposite fibres, *Sci. Rep.* 7 (2017) 4090.

[49] A. Ishikawa, T. Takata, J.N. Kondo, M. Hara, H. Kobayashi, K. Domen, Oxysulfide Sm<sub>2</sub>Ti<sub>2</sub>S<sub>2</sub>O<sub>5</sub> as a stable photocatalyst for water oxidation and reduction under visible light irradiation ( $\lambda \leq 650$  nm), *J. Am. Chem. Soc.* 124 (2002) 13547–13553.